



**QUEEN'S
UNIVERSITY
BELFAST**

Toward Rapid Transient Identification and Characterization of Kilonovae

Coughlin, M., Dietrich, T., Kawaguchi, K., Smartt, S., Stubbs, C., & Ujevic, M. (2017). Toward Rapid Transient Identification and Characterization of Kilonovae. *The Astrophysical Journal*, 849(1), Article 12. <https://doi.org/10.3847/1538-4357/aa9114>, <https://doi.org/10.3847/1538-4357/aa9114>

Published in:
The Astrophysical Journal

Document Version:
Publisher's PDF, also known as Version of record

Queen's University Belfast - Research Portal:
[Link to publication record in Queen's University Belfast Research Portal](#)

Publisher rights
© 2017 The American Astronomical Society.
This work is made available online in accordance with the publisher's policies. Please refer to any applicable terms of use of the publisher.




General rights
Copyright for the publications made accessible via the Queen's University Belfast Research Portal is retained by the author(s) and / or other copyright owners and it is a condition of accessing these publications that users recognise and abide by the legal requirements associated with these rights.

Take down policy
The Research Portal is Queen's institutional repository that provides access to Queen's research output. Every effort has been made to ensure that content in the Research Portal does not infringe any person's rights, or applicable UK laws. If you discover content in the Research Portal that you believe breaches copyright or violates any law, please contact openaccess@qub.ac.uk.

Open Access
This research has been made openly available by Queen's academics and its Open Research team. We would love to hear how access to this research benefits you. – Share your feedback with us: <http://go.qub.ac.uk/oa-feedback>



Toward Rapid Transient Identification and Characterization of Kilonovae

Michael Coughlin¹ , Tim Dietrich², Kyohei Kawaguchi², Stephen Smartt³ , Christopher Stubbs^{1,4} , and Maximiliano Ujevic⁵

¹Department of Physics, Harvard University, Cambridge, MA 02138, USA

²Max Planck Institute for Gravitational Physics, Albert Einstein Institute, D-14476 Golm, Germany

³Astrophysics Research Centre, School of Mathematics and Physics, Queen's University Belfast, Belfast BT7 1NN, Northern Ireland, UK

⁴Department of Astronomy, Harvard University, Cambridge, MA 02138, USA

⁵Centro de Ciencias Naturais e Humanas, Universidade Federal do ABC, 09210-580, Santo Andre, Sao Paulo, Brazil

Received 2017 August 25; revised 2017 October 2; accepted 2017 October 2; published 2017 October 25

Abstract

With the increasing sensitivity of advanced gravitational-wave (GW) detectors, the first joint detection of an electromagnetic and GW signal from a compact binary merger will hopefully happen within this decade. However, current GW likelihood sky areas span $\sim 100\text{--}1000\text{ deg}^2$, and thus it is a challenging task to identify which, if any, transient corresponds to the GW event. In this study, we make a comparison between recent kilonova/macronova light-curve models for the purpose of assessing potential light-curve templates for counterpart identification. We show that recent analytical and parameterized models for these counterparts result in qualitative agreement with more complicated radiative transfer simulations. Our analysis suggests that with improved light-curve models with smaller uncertainties it will become possible to extract information about ejecta properties and binary parameters directly from the light-curve measurement. Even tighter constraints are obtained in cases for which GW and kilonova parameter estimation results are combined. It will therefore be important to make comparisons and potentially combine parameter estimation with the kilonova and GW results. However, to be prepared for upcoming detections, more realistic kilonova models are needed. These will require numerical relativity with more detailed microphysics, better radiative transfer simulations, and a better understanding of the underlying nuclear physics.

Key words: gravitational waves – stars: neutron – surveys

1. Introduction

The recent discovery of compact binary black hole systems (Abbott et al. 2016b, 2016c, 2017) has initiated the era of gravitational-wave (GW) astronomy and even enhanced the interest in the combined observation of an electromagnetic (EM) and a GW signal (Abbott et al. 2016a). Currently, GW sky maps contain likelihood sky areas spanning $\sim 100\text{--}1000\text{ deg}^2$ (Fairhurst 2009; Wen & Chen 2010; Fairhurst 2011; Grover et al. 2014; Sidery et al. 2014; Singer et al. 2014; Berry et al. 2015); thus, it is essential to be able to differentiate transients associated with GW events from other transients. Models for potential EM emission from compact binary mergers remain highly uncertain, but emission timescales ranging from seconds to months and wavelengths from X-ray to radio can be expected (Nakar 2007; Metzger & Berger 2012).

Due to the large uncertainties in the sky localizations from the GW detectors, wide-field survey telescopes are needed to enable an optical and near-infrared EM follow-up study. Examples of current and future wide-field telescopes are the Panoramic Survey Telescope and Rapid Response System (Pan-STARRS; Morgan et al. 2012), the Asteroid Terrestrial-impact Last Alert System (Tonry 2011), the intermediate Palomar Transient Factory (PTF; Rau et al. 2009), what will become the Zwicky Transient Facility (ZTF), and the Large Synoptic Survey Telescope (Ivezic et al. 2008).

There are a variety of automatic schemes in surveys such as iPTF/ZTF (Kasliwal et al. 2016) and Pan-STARRS (Smartt et al. 2016a) trying to determine which transients are unassociated with the GW trigger. For example, asteroids, variable stars, and active galactic nuclei are all objects that form the background for these searches and therefore have to be removed (Cowperthwaite & Berger 2015). In general,

background supernovae are the transients that remain after these cuts. To further reduce the number of candidates, transients with host galaxies beyond the reach of the GW detectors are also removed. In addition, photometric evolution can be used to discriminate recent transients from old supernovae. After spectra are taken, they are cross-matched against a library of supernovae, where they can be classified as Type Ia supernovae (SNe Ia), two hydrogen-rich core-collapse supernovae (SNe II), active galactic nuclei, etc. The remaining transients that could not be identified might then be connected to the GW trigger.

A variety of potential EM counterparts have been theorized to accompany the GW detection of a compact binary containing at least one neutron star, e.g., short gamma-ray bursts, kilonovae, or radio bursts. Among the most promising “smoking guns” of GW detections are kilonovae (also called macronovae; Metzger & Berger 2012). Kilonovae are produced during the merger of a binary neutron star (BNS) or a black hole–neutron star (BHNS) system, generating EM radiation by the decay of r -process ions produced and ejected during the merger. They last over a week, peak in the near-infrared with luminosities $\approx 10^{40}\text{--}10^{41}\text{ erg s}^{-1}$ (Barnes & Kasen 2013; Metzger et al. 2015), and are powered by the decay of radioactive r -process nuclei in the ejected material produced during the compact binary merger; see Metzger (2017) and Tanaka (2016) for recent reviews (for a review about multi-messenger astronomy, see also Rosswog 2015). Some studies point out that the electromagnetic emissions similar to kilonovae can also be produced in different mechanisms (Kyutoku et al. 2014; Kisaka et al. 2015). Material is ejected because of processes such as torque inside the tidal tails of the neutron stars, high thermal pressure produced by shocks

created during the collision of two neutron stars, and neutrino- or magnetic-field-driven winds. In reality, different ejecta mechanisms act simultaneously, producing unbound material with complex morphology and composition.

To model kilonova properties as realistically as possible, full numerical relativity (NR) simulations and radiative transfer simulations have to be combined. NR simulations are needed to study the merger process and the different ejecta mechanisms. However, because those simulations only cover about a few hundred milliseconds around the compact binary merger, our knowledge about ejecta mechanisms acting on a longer timescale, due to magnetic-field-driven winds, etc., is still limited (e.g., Siegel & Metzger 2017). Once the ejecta properties (ejecta mass, velocity, composition, morphology) are extracted from full NR simulations, this information can be used to set up radiative transfer simulations from which the light curve of the kilonova can be computed. However, because of the complexity of NR and radiative transfer simulations, and due to our ignorance of astrophysical processes acting during the merger and postmerger of two compact objects, a variety of kilonova approximants exist.

In this paper, we shortly review some of the existing kilonova models. In particular, we will compare the parameterized models of Kawaguchi et al. (2016) and Dietrich & Ujevic (2017) against themselves and other kilonova/macronova models and radiative transfer simulations (Tanaka et al. 2014; Barnes et al. 2016; Rosswog et al. 2017). We ask the question of how much the models vary in their own parameters, using parameter estimation techniques to show plausible posteriors in case of a counterpart detection. We will study how robust they are in terms of approximating other light curves and briefly compare the parameterized models to an example of a background contaminant, SN Ia using the SALT2 spectrophotometric empirical model (Guy et al. 2007). We explore the parameter degeneracies that arise from measurement of ejecta mass and velocity, M_{ej} and v_{ej} , including the interplay between the measurement of masses and neutron star compactness. We then consider the potential benefits of joint GW and EM parameter estimation.

2. Motivation

It is reasonable to question the purpose of parameter estimation of light curves with models that still might miss important astrophysical processes and that have systematic errors. Let us envision that we have a light curve from a transient consistent with both the time of the GW trigger and the skymap. There have been a number of cases where transients have been identified with these parameters, and it was necessary to determine their potential association with the GW event (Smartt et al. 2016a, 2016b; Stalder et al. 2017). In this way, there is a significant benefit to be able to show consistency between a measured light curve and an expected model to lend credibility to the association between the GW and EM trigger.

This is similar to the case of the first GW detection (which did not have an identified EM counterpart), where parameter estimation did not play a leading role in the assessment of the significance but was important for verification that the detection was indeed real.

Furthermore, for the ideal case in which a well-sampled light curve, mass posteriors from LIGO measurements, and a

distance estimate from a host galaxy are available, we can use the distance from the host and convert apparent into absolute magnitudes. For such a case and with the availability of trustworthy models, we do not need to allow for any zero-point or time offset and would be able to place stringent constraints on the binary parameters directly from the kilonova measurement.

Finally, with significantly improved kilonova models based on more accurate NR and radiative transfer simulations, including improved knowledge about nuclear physical properties, it might become possible to directly extract information of the compact binary from a well-sampled light curve from a kilonova counterpart measured in multiple bands, e.g., by a telescope such as Pan-STARRS. This would allow for access to the properties of individual compact binary mergers even in the case where no GW signal or only a single detector trigger was present.

3. Models

3.1. Kilonova Models

As pointed out, to perform accurate NR and radiative transfer simulations remains a challenging task, and further work including a better microphysical treatment is needed to allow a detailed understanding of ejecta, r -processes, and EM emission. In the following, we give a brief overview about some approaches without guarantee of completeness.

There are two major classes of kilonova models, those that model dynamic ejecta and those that model winds. Historically, kilonovae from dynamical ejecta were proposed earlier than those from wind kilonova. In this paper, we use parameterized models that concentrate on dynamic ejecta (Kawaguchi et al. 2016; Dietrich & Ujevic 2017), although the technique is generic enough to use wind models as well. It will be important when using this method on a transient to either include a wind model in addition to a dynamic ejecta model or, perhaps better, include one capable of incorporating both, such as the toy model in Metzger (2017).

One model is driven by the merger of two neutron stars, where material ejected during or following the merger assembles into heavy elements by the r -process (Metzger et al. 2010). Kulkarni (2005) postulated that ^{56}Ni or free neutrons provided the power to these events, although ^{56}Ni cannot be produced in the neutron-rich environments (Metzger 2017). Li & Paczynski (1998) first pointed out that radioactive ejecta from compact binary mergers are a source of electromagnetic emission. Metzger et al. (2010) used radioactive heating rates derived from r -process nuclear network calculations to determine the correct luminosity scale for the corresponding light curves. Kasen et al. (2013) then pointed out the high opacities of the resulting Lanthanides, with Barnes & Kasen (2013) and Tanaka & Hotokezaka (2013) performing the first realistic simulations for kilonova light curves.

EM emission then occurs during the radioactive decay of the resulting nuclei. Barnes et al. (2016) explore the emission profiles of the radioactive decay products, which include nonthermal β -particles, α -particles, fission fragments, and γ -rays, and the efficiency with which their kinetic energy is absorbed by the ejecta. By determining the net thermalization efficiency for each particle type and implementing the results into detailed radiation transport simulations, they provide kilonova light-curve predictions. Metzger et al. (2015) also

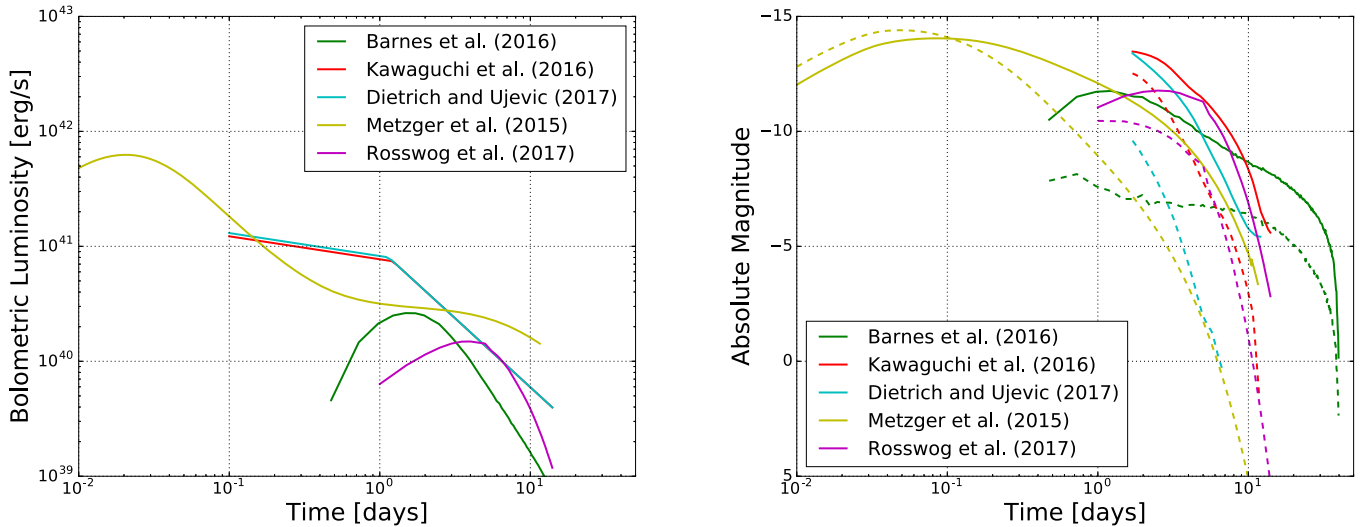


Figure 1. Bolometric luminosity (left) and light curves in the g (dashed) and i (solid) bands (right). The parameterized models of Kawaguchi et al. (2016) and Dietrich & Ujevic (2017) use $M_{\text{ej}} \approx 5 \times 10^{-3}$, $v_{\text{ej}} \approx 0.2$, and $\theta = 0.2$ rad. Barnes et al. (2016) use a model with $M_{\text{ej}} \approx 5 \times 10^{-3}$ and $v_{\text{ej}} \approx 0.2$. We use the fiducial model of Metzger et al. (2015), which uses a neutron mass cut $m_n = 10^{-4}$, opacity of $\kappa = 30 \text{ cm}^2 \text{ g}^{-1}$, and electron fraction $Y_e = 0.05$. From Rosswog et al. (2017), we include a model with $M_{\text{ej}} = 0.0079$ and $v_{\text{ej}} = 0.12$, which is the closest available to our fiducial model.

explore the β -decay of the ejecta mass powering a “precursor” to the main kilonova emission, which peaks on a timescale of a few hours in the blue. Rosswog et al. (2017) use semianalytical models based on nuclear network simulations studying in detail the effect of the nuclear heating rate and ejecta electron fraction. The work of Rosswog et al. (2017) shows in detail how light-curve predictions change significantly for different nuclear physics parameters, e.g., the usage of different mass models.

Another kilonova mode, also driven by the r -process, in which radioactively powered transients are produced by accretion disk winds after the compact object merger was proposed by Kasen et al. (2015). In this model, the light curves contain two distinct components consisting of a ≈ 2 -day blue optical transient and ≈ 10 -day infrared transient. For this model, mergers resulting in a longer-lived neutron star or a more rapidly spinning black hole result in a brighter and bluer transient.

In addition to the numerical work, a handful of analytical models have also been developed with the purpose of approximating kilonova light curves. Based on NR simulations, Kawaguchi et al. (2016) derive fitting formulas for the mass and the velocity of ejecta from a generic BHNS merger and combine this with an analytic model of the kilonova light curve based on the radiative Monte Carlo (MC) simulations of Tanaka et al. (2014). Dietrich & Ujevic (2017) expand this work by using a large set of NR simulations to explore the EM signals from BNSs. The NR fit estimating the ejecta mass, velocity, and morphology is extended by an analytical model also based on the radiative MC simulations of Tanaka et al. (2014).

Parameterized models as proposed in Kawaguchi et al. (2016) and Dietrich & Ujevic (2017) directly tie GW parameters to expectations about the potential kilonova counterpart. They do not require NR and radiative transfer simulations to be completed, which is an impossible task over the few days of observations. Assumptions about the equation of state (EOS) of neutron stars, as well as measurement of the mass of the compact objects involved, allow the computation of the luminosity and light curves of kilonovae.

3.2. Luminosity Predictions

Because the ejecta morphology, the thermalization efficiency, and the opacity are not well constrained, it is advantageous to use a variety of models that estimate these quantities in different ways. In general, the luminosity will depend on the thickness of the ejecta, which is one of the main differences between BNS and BHNS systems. The thinner the ejecta becomes, the higher the density and temperature become. This affects the color temperature of the spectrum and consequently has a large impact on the detected light curve.

There are two limiting cases: (i) the ejecta are geometrically thick and approximately spherical, and (ii) the ejecta are geometrically thin. In general, due to shock-driven ejecta, BNS mergers correspond mostly to the former case and BHNS systems to the latter case; however, a clear distinction is impossible. The morphology of ejecta affects the diffusion timescale and changes the evolution of the light curve before the system becomes optically thin. When the system is optically thin, the difference in morphology may not be important for the light-curve evolution anymore. Since information about ejecta velocity is primarily contained in the light curve during the optically thick phase, modeling of this phase is important to constrain ejecta velocity.

As a first comparison between different models, we consider spherical ejecta with $M_{\text{ej}} \approx 5 \times 10^{-3}$ and $v_{\text{ej}} \approx 0.2$ (see Barnes et al. 2016). Here and in the following, we give v_{ej} in fractions of the speed of light and masses in fractions of the mass of the Sun M_{\odot} . For the nonspherical parameterized models of Kawaguchi et al. (2016) and Dietrich & Ujevic (2017), we further assume $\theta = 0.2$ rad. From Rosswog et al. (2017), we include a model with $M_{\text{ej}} = 0.0079$ and $v_{\text{ej}} = 0.12$, which is closest to our fiducial model.

Additionally, we include the approximant of Metzger et al. (2015), which focused on the blue transient produced at a time around merger, which uses a neutron mass cut $m_n = 10^{-4}$, opacity of $\kappa = 30 \text{ cm}^2 \text{ g}^{-1}$, and electron fraction $Y_e = 0.05$.

Figure 1 shows the bolometric luminosity and the light curves in the g (dashed) and i (solid) bands. The kilonova models have significant short-term dynamics, with changes of

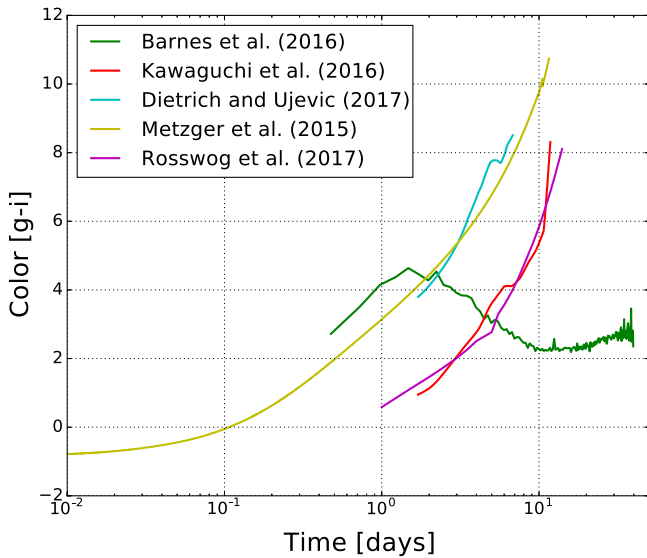


Figure 2. Difference between the g and i bands for the models presented in Figure 1.

more than a magnitude in less than a day. Both the Kawaguchi et al. (2016) and Dietrich & Ujevic (2017) models are based on the MC simulations of Tanaka et al. (2014), for which a constant thermal efficiency is assumed ($\epsilon_{\text{th}} = 0.5$).

The model of Barnes et al. (2016) includes a time-dependent efficiency, which leads to a faster decay of the bolometric luminosity and magnitude because after a few days after the merger the thermalization efficiency drops below the constant thermalization efficiency employed in the Tanaka et al. (2014) simulations. Rosswog et al. (2017) employ both time-dependent and constant efficiencies and use a more complex density profile. The model picked from Rosswog et al. (2017) shows a smaller bolometric luminosity than other models; notice, however, that as shown in Rosswog et al. (2017), the usage of different mass models affects the luminosity by about $\approx 600\%$, i.e., all presented models come with large uncertainties and are crucially dependent on nuclear physics assumptions. The model of Metzger et al. (2015) describes the blue transient arising from a small fraction of the ejected mass that expands sufficiently rapidly such that the neutrons are not captured and instead β -decay, giving rise to a clear peak in the bolometric luminosity visible around the time of merger.

Comparing Dietrich & Ujevic (2017) and Kawaguchi et al. (2016), we see a clear difference in the g band. This has already been pointed out in Tanaka et al. (2014). The main difference seems to arise from the difference of employed bolometric corrections, which itself will depend on the ejecta morphology. Since BHNS ejecta are much more nonspherical and are concentrated in the equatorial plane, they have higher temperatures that make the spectrum bluer than BNS ejecta with the same mass.

We can take the opportunity of having a variety of kilonova models accessible to compare the light-curve colors. It is common in dedicated searches for kilonovae to make color cuts (Doctor et al. 2017). Figure 2 shows the difference between the g and i bands for the models presented in Figure 1. As expected, all of the kilonova models show differences of at least 2 mag, especially on later timescales. For this reason, independent of the employed kilonova model, the proposed analysis will optimize the strategy for the detection of GW

optical counterparts. Given the relative consistency in color among the models, imaging the transients in both the blue/green and the near-infrared can help differentiate from other transients. Due to the high opacities of Lanthanide elements, most models predict emission in the near-infrared wavelengths. These observations are required within the first few days owing to the faint magnitudes involved. As explained above, the significant changes in magnitude over day timescales can also help differentiate them as compared to possible background transients such as SNe Ia.

3.3. Dependence of the Bolometric Light Curve on the Density Profile, Morphology, and Thermal Efficiency

As shown in Figure 1 (left panel), the bolometric luminosity of the models from Kawaguchi et al. (2016), Dietrich & Ujevic (2017), Barnes et al. (2016), and Rosswog et al. (2017) can be significantly different (we do not include the blue transient proposed in Metzger et al. [2015] in the following analysis since it is powered by a different mechanism). While similar ejecta masses, velocities, and energy deposition rates are employed, the models use different density profiles, morphology, and thermalization efficiency. The models of Kawaguchi et al. (2016) and Dietrich & Ujevic (2017) assume $\rho \propto r^{-2}$ for the density profile, nonspherical geometry, and a constant thermalization efficiency ($\epsilon_{\text{th}} \approx 0.5$). The model of Barnes et al. (2016) assumes spherical ejecta with $\rho \propto r^{-1}$ for the density profile, and the time-dependent (mass-dependent) thermalization efficiency is taken into account. The model of Rosswog et al. (2017) also assumes spherical ejecta with a homogeneously expanding density profile and time-dependent (mass-dependent) thermalization efficiency with the FRDM model.

To check how these differences affect the bolometric light curves, we perform a simple radiation transfer simulation varying the density profile, ejecta morphology, and thermalization efficiency. In this calculation, we assume the flux-limited diffusion approximation of the radiative transfer (Levermore & Pomraning 1981), a constant gray opacity with $10 \text{ cm}^2 \text{ g}^{-1}$, and the heating rate that is employed in Kawaguchi et al. (2016) and Dietrich & Ujevic (2017).

Figure 3 compares the bolometric luminosity for various setups. The figure clearly shows that different ejecta morphologies and thermalization efficiencies change the bolometric luminosity by a factor of ≈ 2 . This explains qualitatively the difference in the bolometric luminosity and light curves in Figure 1. The difference in the model of Rosswog et al. (2017) is also explained by the difference in the ejecta mass, ejecta velocity, and thermalization efficiencies. On the other hand, a different density profile has only a minor effect.

These results indicate that for future development of analytical kilonova approximants the focus should be put on modeling the ejecta morphology and the time-dependent thermalization efficiency. We also find that considering a constant thermalization efficiency of $\epsilon_{\text{th}} = 1$ and then multiplying by $\epsilon_{\text{th}}(t)$ (given in Barnes et al. 2016) or directly employing a time-dependent thermal efficiency leads only to differences of $\approx 40\%$. This suggests that, at least for the bolometric luminosity, the time dependency of the thermalization efficiency can be approximately taken into account just by multiplying its function by the luminosity obtained by the constant efficiency. This is of particular importance for further improvement of the parameterized models, which, at the

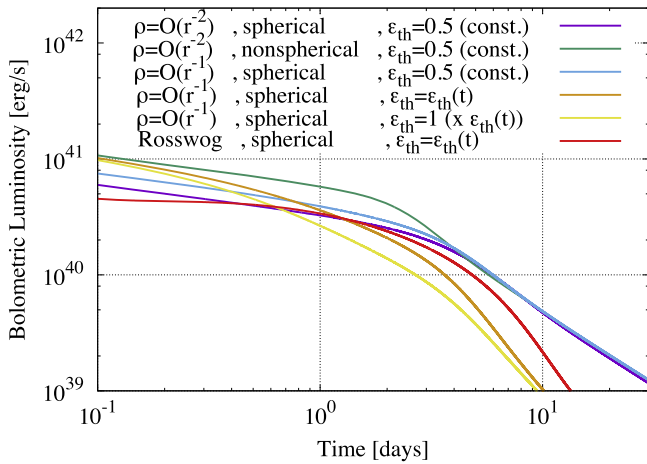


Figure 3. Comparison of the bolometric luminosity for various setups. The purple line employs a $\rho \propto r^{-2}$ density profile, spherical geometry, and a constant thermalization efficiency ($\epsilon_{\text{th}} \approx 0.5$). The green line is similar to the purple curve but with nonspherical ejecta with $\theta_{\text{ej}} = 0.2$ and $\varphi = \pi$ (the same morphology employed in Kawaguchi et al. 2016; Dietrich & Ujevic 2017; Barnes et al. 2016). The blue curve is similar to the purple curve but with a $\rho \propto r^{-1}$ density profile. The orange line is similar to the blue one but with the time-dependent (mass-dependent) thermalization efficiency of Barnes et al. (2016). The yellow curve is similar to the blue curve, but we employed a constant thermalization efficiency ($\epsilon_{\text{th}} = 1$) and multiplied afterward by the time-dependent (mass-dependent) thermalization efficiency given in Barnes et al. (2016). The red curve denotes the bolometric light curve employing $M_{\text{ej}} = 0.0079$ and $v_{\text{ej}} = 0.12$ and the same density profile as in Rosswog et al. (2017).

current stage, are based on simulations employing a constant thermalization efficiency.

In addition to the discussed effects, further uncertainties exist, which make a modeling and prediction of kilonova luminosities difficult. Rosswog et al. (2017) point out that the electron fraction and heating rate are main uncertainties in the current modeling of kilonova light curves. They find that by using two different mass models (DZ31, Duflo & Zuker 1995; Finite Range Droplet Model, Moller et al. 1995) the bolometric luminosity can be different up to $\approx 600\%$. This is caused by the fact that the nuclear heating rate enters linearly into the bolometric luminosity.

4. Model Comparisons and Parameter Estimation

In this section, we perform parameter estimation and model comparisons. We will use the Kawaguchi et al. (2016) and Dietrich & Ujevic (2017) models to compare both to other models and against themselves. As described, there are two parts to each of these models: the ejecta fitting formulae and the kilonova light curves. Avoiding the ejecta fitting formulae, we can improve efficiency and accuracy by directly sampling the ejecta mass M_{ej} and velocity v_{ej} and later employ the correlations between the ejecta mass properties, e.g., ejecta mass M_{ej} and velocity v_{ej} and the binary parameters (see Section 5). Furthermore, we sample over the latitudinal and longitudinal opening angles, denoted as θ_{ej} and ϕ_{ej} , respectively. Opacity $\kappa = 10 \text{ cm}^2 \text{ g}^{-1}$, heating rate coefficient $\epsilon_0 = 1.58 \times 10^{10} \text{ erg g}^{-1} \text{ s}^{-1}$, heating rate $\alpha = 1.2$, and thermalization efficiency $\epsilon_{\text{th}} = 0.5$ are held fixed. The heating rate coefficient ϵ_0 and the power of the heating rate α are combined such that the specific heating for energy release caused by radioactive decay can be approximated by $\dot{\epsilon} = \epsilon_0 (t/1 \text{ day})^{-\alpha}$ (Dietrich & Ujevic 2017).

In this analysis, we will use a version of Multinest (Feroz et al. 2009b) commonly used in GW data analysis (Feroz et al. 2009a) and wrapped in python (Buchner et al. 2014). This algorithm has the benefit of computing the Bayesian evidence for a given set of parameters, which can be used to assign relative probabilities to different models. The likelihood evaluation proceeds as follows. For each parameter set sampled, light curves in *griz* bands are computed. We use linear extrapolation of the magnitudes to extend the light curves in cases where the model does not predict the full time covered by the target light curve. In addition to the parameters above, we also allow the light curves to shift in time by an offset T_0 , which allows for a measurement of the initial time of the kilonovae and therefore gives important evidence for a potential counterpart, and in magnitude by a color-independent zero-point offset ZP, which compensates for our ignorance about the distance to the source. This does not prevent the estimation of M_{ej} because M_{ej} changes both the timescale of the fade and the luminosity (v_{ej} can also change the timescale of the bolometric luminosity but not that of the bolometric correction for our current implementation, which should also be tested when the model is improved). A χ^2 distribution is then calculated between the light curve produced from the model and the target light curve. The likelihood is then simply that from a χ^2 distribution. The priors used in the analyses are as follows: $-5 \leq T_0 \leq 5$ days, $-50.0 \leq \text{ZP} \leq 50.0$ mag, $-5 \leq \log_{10}(M_{\text{ej}}) \leq 0$, $0 \leq v_{\text{ej}} \leq 1$, $0 \leq \theta \leq \pi/2$ rad, and $0 \leq \phi \leq 2\pi$ rad. The priors are flat over the stated ranges.

4.1. Self-consistency Check of Parameterized Models

As a first test of the numerical method, we use light curves produced by the parameterized models for BNS and BHNS and also recover the ejecta properties with the same models. The top row of Figure 4 shows light curves of such a comparison, where we assume uncertainties of the models of 1 mag as stated in Dietrich & Ujevic (2017) and Kawaguchi et al. (2016). The top row shows that the injected light curves are recovered properly. We quantify the level of overlap between parameters with “corner” plots (Foreman-Mackey 2016), shown in the bottom row of Figure 4. Shown are 1D and 2D posteriors marginalized over the rest of the parameters. In general, there are a few key features. First, with the ≈ 1 mag uncertainty associated with these models, a large number of light curves computed with the parameterized models are consistent with the injected/baseline light curve we took. This means that no strict parameter constraints can be obtained. However, although the models have stated ≈ 1 mag uncertainty, we can study a possible scenario with models having smaller uncertainties, e.g., ≈ 0.2 mag or even 0.04 mag, which approximate the characteristic uncertainty for observations. In Figure 5, we show histograms for M_{ej} for the case where the uncertainties are varied. The figure demonstrates that M_{ej} constraints are significantly improved when the assigned error to the model is small. In particular, for an uncertainty of 0.2 mag the ejecta mass can be determined up to $\log_{10} M_{\text{ej}} \approx \pm 0.5$, and in cases where the uncertainty would be limited by the observation (uncertainty of 0.04 mag) the ejecta mass could be determined to $\log_{10} M_{\text{ej}} \approx \pm 0.1$. This motivates the need for further improved parameterized models of kilonova light curves.

In contrast to the ejecta mass, the ejecta velocity is poorly constrained in our analysis. This is because the analytic models do not include times $t \lesssim 1$ day, where the ejecta are optically

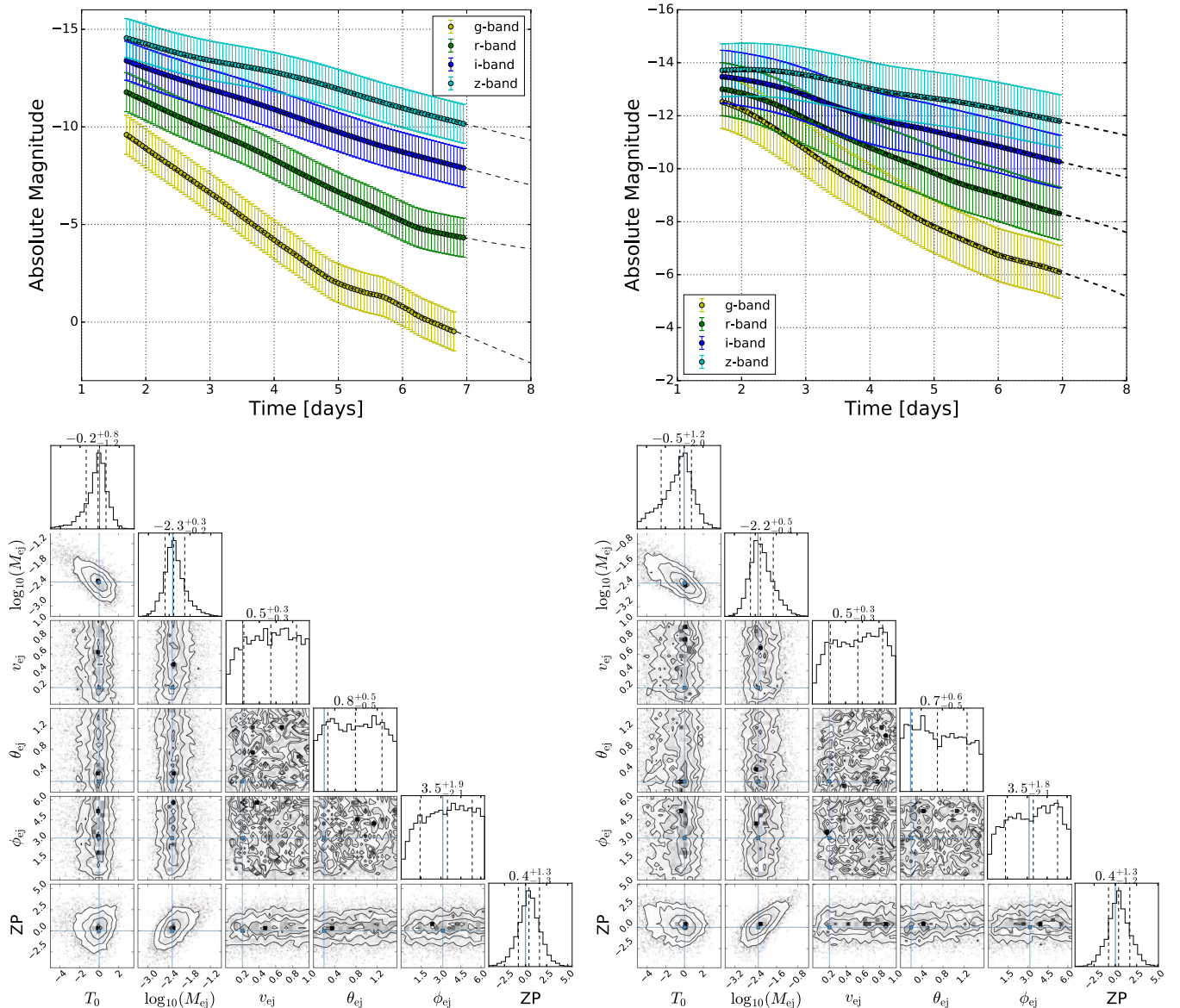


Figure 4. Top row: light curves for Dietrich & Ujevic (2017; left) and Kawaguchi et al. (2016; right). We use light curves with $M_{ej} = 5 \times 10^{-3}$, $v_{ej} = 0.2$, $\theta_{ej} = 0.2$ rad, and $\phi_{ej} = 3.14$ rad for the light-curve computation. We also perform a maximum likelihood χ^2 fit to each light curve using the same models for comparison. The lines with error bars show the injected light curve with the assumed 1 mag error budget. The dashed black lines show the best-fit light curve to that model, including the linear extrapolation. Bottom row: corresponding corner plots.

thick. However, the dependence on the ejecta velocity is only significant during this stage. Afterward, the light curves are primarily determined by the ejecta mass. Therefore, to improve the estimation of the ejecta velocity, extension of the light-curve models to earlier times is required.

4.2. Comparison with Tanaka et al.

We now perform a comparison between the parameterized models and results from Tanaka et al. (2014). In this and the following subsections, as we are using models that differ from the light curves they are being compared to, there will be a bias above and beyond the statistical uncertainty from sampling over the model parameter space. We will report the statistical uncertainty in the following sections and compare the statistical uncertainty to the true values to estimate bias. As discussed above, the models differ in the thermalization efficiency, opacity calculations, density profiles, and in other ways, and

these differences lead to light-curve differences and therefore biases in the parameter estimation. Therefore, the models effectively have larger error bars than the 1 mag error stated in Kawaguchi et al. (2016) and Dietrich & Ujevic (2017).

For this analysis, we distinguish between BNS and BHNS. The BNS setups of Tanaka et al. (2014) are compared to the Dietrich & Ujevic (2017) model, and the BHNS light curves are compared to the Kawaguchi et al. (2016) model. In Figure 6, we show histograms for M_{ej} for uncertainties of 1 mag (dot-dashed lines). The ejecta mass corresponding to the light curves of Tanaka et al. (2014) (vertical dashed lines) is always within the posteriors of the models for the 1 mag posteriors (dot-dashed lines). We find that for 0.2 mag (solid lines) uncertainties some of the true values for BNS systems lie outside the estimated posteriors, which is to be expected because the uncertainties in Dietrich & Ujevic (2017) and Kawaguchi et al. (2016) are 1 mag. But, even for an assigned

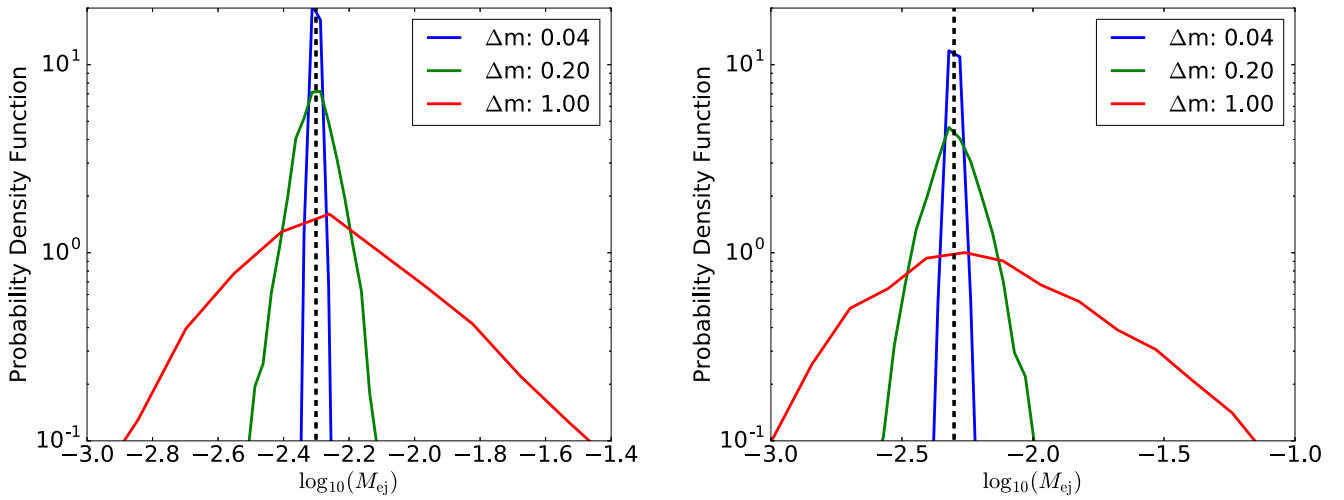


Figure 5. Histograms of M_{ej} recovery. We inject light curves computed with the parameterized model of Dietrich & Ujevic (2017; left) and Kawaguchi et al. (2016; right). We recover the injected light curve with the same model. For decreasing uncertainties assigned to the models, the ejecta mass gets better constrained and approaches the true value (vertical dot-dashed line).

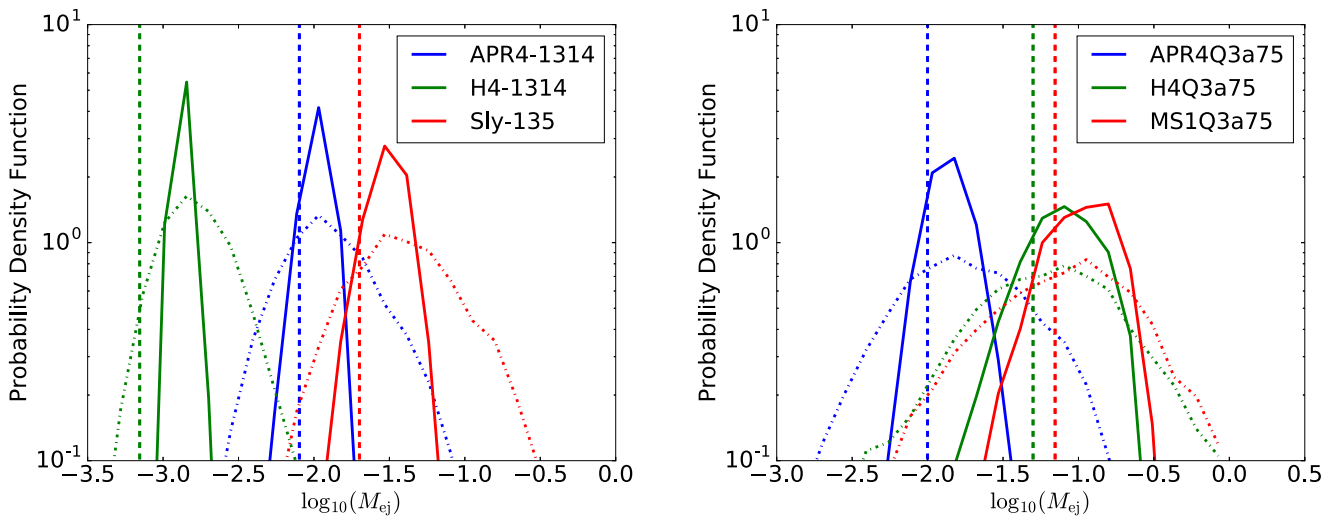


Figure 6. Histograms of M_{ej} for the BNS and BNHS light curves from Tanaka et al. (2014) compared with the Dietrich & Ujevic (2017) model (left) and Kawaguchi et al. (2016) model (right), respectively. For this analysis, there are errors of 0.2 mag (solid lines) and errors of 1 mag (dot-dashed lines).

uncertainty of 0.2 mag, the posteriors of the BHNS setups are consistent with the injected values, which suggests that recovering smaller ejecta masses are in general less accurate (or equivalently have more bias). This might be caused by inaccuracies in the employed bolometric corrections and is already visible in Figure 9 of Dietrich & Ujevic (2017).

4.3. Comparison with Other Kilonova Models

We now perform a comparison between the parametric models and those of Barnes et al. (2016) and Rosswog et al. (2017). In Figure 7, we take the Barnes et al. (2016) (top panel) model `rpft_m005_v2` and the NS12NS12 FRDM model of Rosswog et al. (2017) (bottom panel) and use the Dietrich & Ujevic (2017) model for recovery. One finds that the relative magnitudes between the bands are mostly consistent across the models. However, the models are not able to reproduce the light curves as accurately as for Tanaka et al. (2014). We find that multiple parameters cannot be constrained, while the ejecta mass, shown in Figure 8, is overestimated. Furthermore, for Rosswog et al. (2017) the parameter estimation pipeline leads

to a T_0 estimate of the order of a few days, which suggests that follow-up searches using the current parameterized models would not correctly detect transients with light curves similar to those given in Rosswog et al. (2017).

The origin of the difference between the parameterized models and those of Barnes et al. (2016) and Rosswog et al. (2017) is that Dietrich & Ujevic (2017) was built using the light curves of Tanaka et al. (2014). It can be expected that parameterized models approximating the results of Barnes et al. (2016) and Rosswog et al. (2017) can be obtained as well. This shows that for future development, it is urgently required to provide light curves using full radiative transfer simulations that are as realistic as possible, i.e., including different ejecta components, time-dependent efficiency, and complex ejecta morphologies.

4.4. Comparison with Other Models

We also compare to a few non-kilonova models in Figure 9. Considering the different origin of the EM signal, we expect that the kilonova models cannot capture the injected light

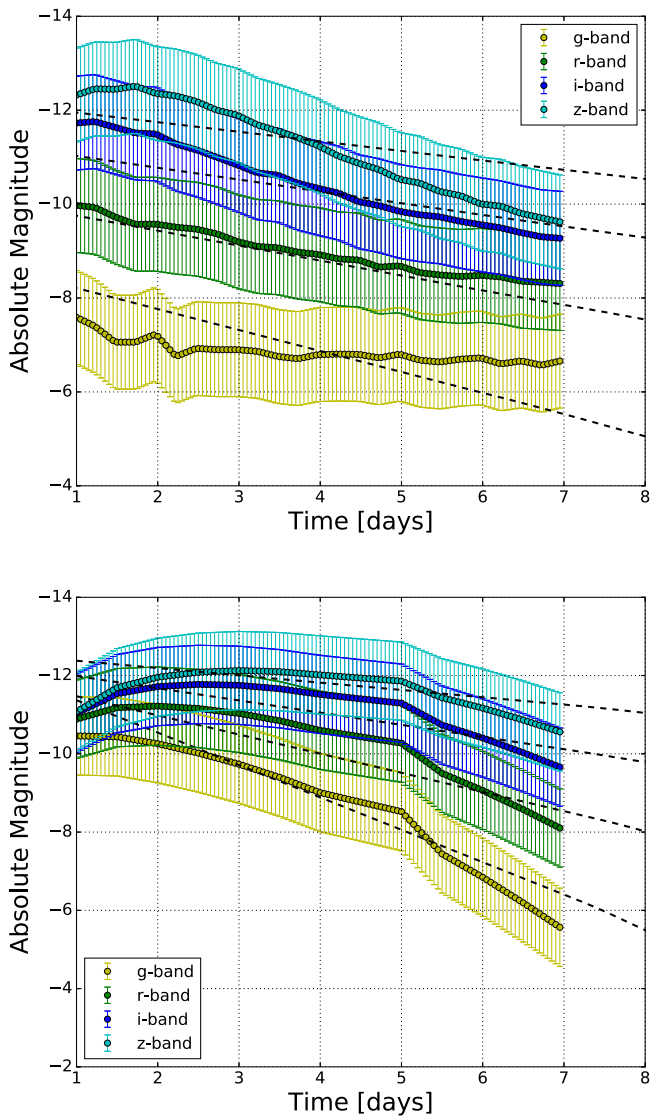


Figure 7. Light curves for Barnes et al. (2016; top) and Rosswog et al. (2017; bottom) with the same parameters as from Figure 1. We also perform a maximum likelihood chi-squared fit to each light curve using the Dietrich & Ujevic (2017) model for comparison.

curves. We use the Metzger et al. (2015) fiducial model (top panel of Figure 9) describing the blue kilonovae precursor and an SN Ia model from Guy et al. (2007) (bottom panel). Metzger et al. (2015) do have an initially higher blue component. The best-fit curve from Dietrich & Ujevic (2017) is capable of producing time-dependent light-curve approximants. For the SN Ia it was not possible to compute time-dependent light curves with the parameterized models that approximate the SN Ia light curve. This shows that the parameterized models can also help to distinguish transients with different origins.

5. Extracting the Binary Parameters

Our previous study focused on the question of how we can use parameterized models to obtain information about the mass, velocity, and morphology of the ejecta. At least as important for astrophysical considerations is the question whether measured light curves can be used to directly constrain the

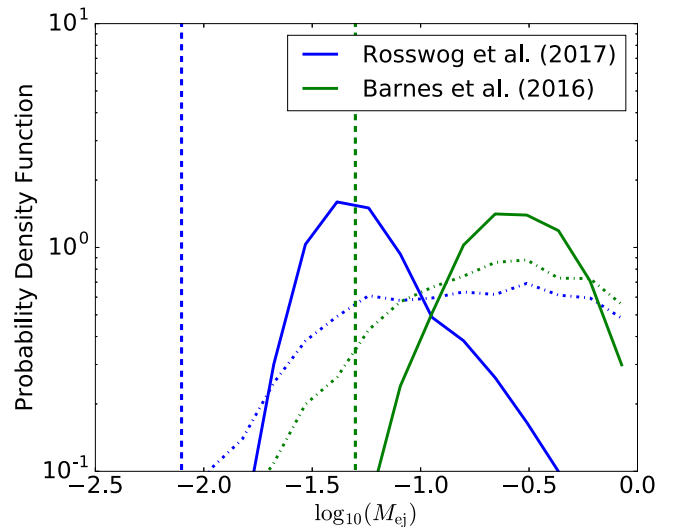


Figure 8. Histogram of M_{ej} recovery for the Barnes et al. (2016) model `rpft_m05_v2` and the NS12NS12 FRDM model of Rosswog et al. (2017) light curves compared with the Dietrich & Ujevic (2017) model (left). For this analysis, there are errors of 0.2 mag (solid lines) and errors of 1 mag (dot-dashed lines).

binary properties: masses, spins, and possibly also the unknown EOS. To achieve this goal, phenomenological models connecting the ejecta properties as well as the binary parameters have to be employed. Such models based on large sets of NR simulations are given in Kawaguchi et al. (2016) for BHNS systems and in Dietrich & Ujevic (2017) for BNS systems. Because of the large uncertainties in the determination of the ejecta mass in full general relativistic simulations, current parameterized models can only be seen as a starting point to more accurate models. Longer simulations with detailed microphysics are needed to properly model all the ejecta components.

5.1. Possible Degeneracies

In addition to the large uncertainty of the NR data, the models also contain degeneracies that do not allow the simultaneous extraction of all binary parameters. The ejecta mass and velocity as functions of the binary parameters for BHNS can be approximated by

$$\frac{M_{\text{ej}}}{M_{\text{NS},*}} = \text{Max} \left\{ a_1 q^{n_1} \frac{1-2C}{C} - a_2 q^{n_2} \tilde{r}_{\text{ISCO}}(\chi_{\text{eff}}) + a_3 \left(1 - \frac{M_{\text{NS}}}{M_{\text{NS}}^*} \right) + a_4, 0 \right\}, \quad (1)$$

$$v_{\text{ej}} = b_1 q + b_2, \quad (2)$$

with $\chi_{\text{eff}} = \chi \cos i_{\text{tilt}}$, where i_{tilt} is the angle between the dimensionless spin of the black hole χ and the orbital angular momentum and \tilde{r}_{ISCO} is the radius of the innermost stable circular orbit normalized by the black hole mass. $a_1, a_2, a_3, a_4, n_1, n_2, b_1, b_2$ are fitting parameters that are determined by comparison to a large set of NR data (see Kawaguchi et al. 2016). For BNS setups, the ejecta properties

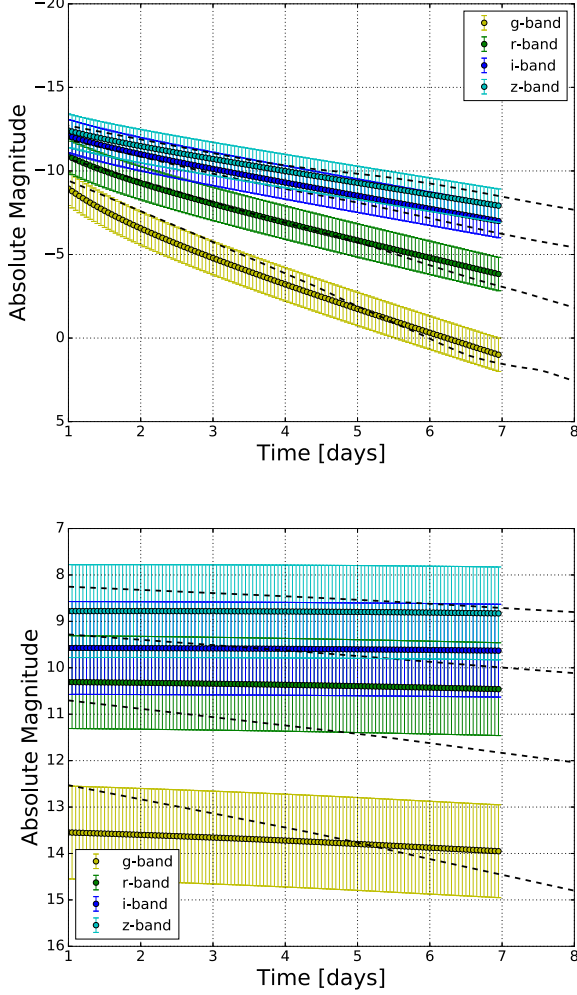


Figure 9. Light curves for Metzger et al. (2015; top), with the same parameters as from Figure 1, and an SN Ia from Guy et al. (2007; bottom). We also perform a maximum likelihood chi-squared fit to each light curve using the Dietrich & Ujevic (2017) model for comparison.

are approximated by

$$M_{\text{ej}}^{\text{fit}} = 10^{-3} \left\{ a \left(\frac{M_2}{M_1} \right)^{1/3} \left(\frac{1 - 2C_1}{C_1} \right) + b \left(\frac{M_2}{M_1} \right)^n + c \left(1 - \frac{M_1}{M_1^*} \right) \right\} M_1^* + (1 \leftrightarrow 2) + d, \quad (3)$$

$$v_{\text{ej}} = \sqrt{v_{\rho}^2 + v_z^2}, \quad (4)$$

$$v_{\rho,z} = \left[a_{\rho,z} \left(\frac{M_1}{M_2} \right) (1 + c_{\rho,z} C_1) \right] + (1 \leftrightarrow 2) + b_{\rho,z}, \quad (5)$$

$$\theta_{\text{ej}} = \frac{2^{4/3} v_{\rho}^2 - 2^{2/3} (v_{\rho}^2 (3v_z + \sqrt{9v_z^2 + 4v_{\rho}^2}))^{2/3}}{(v_{\rho}^5 (3v_z + \sqrt{9v_z^2 + 4v_{\rho}^2}))^{1/3}}, \quad (6)$$

$$\phi_{\text{ej}} = 4\theta_{\text{ej}} + \frac{\pi}{2}, \quad (7)$$

with the fitting parameters $a, b, c, d, a_{\rho}, a_z, b_{\rho}, b_z, c_{\rho}, c_z, n$ given in Dietrich & Ujevic (2017).

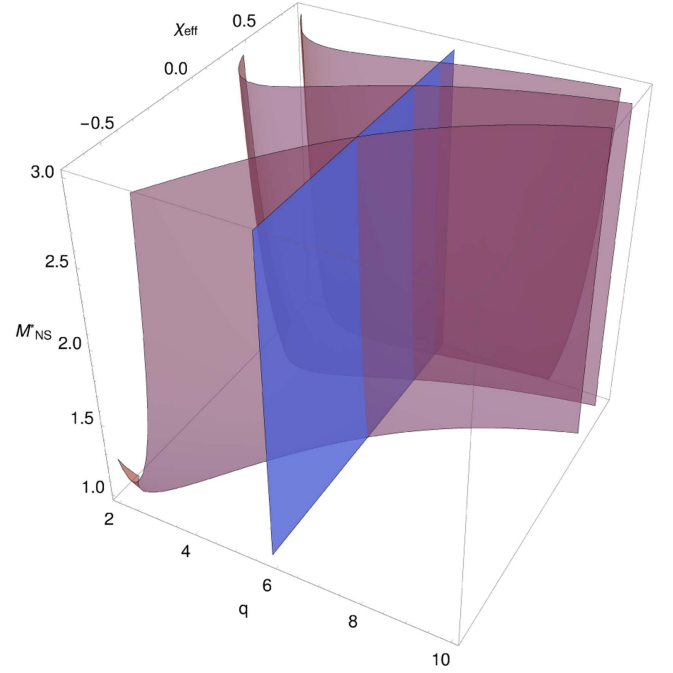


Figure 10. Binary parameters of a BHNS system, Equation (1) and Equation (2), which lead to $M_{\text{ej}} = 10^{-2}$ (red surfaces) and $v_{\text{ej}} = 0.28$ (blue surface) under the assumption of different compactnesses $C = 0.13, 0.15, 0.17$ (from left to right). Because of the degeneracies between the binary parameters and the ejecta properties, an unambiguous measurement of $q, M_{\text{NS}}^*, \chi_{\text{eff}}, C$ is not possible if only M_{ej} and v_{ej} are measured.

As can be concluded from Equations (1)–(7), the BHNS model depends on the mass ratio q , the “effective” spin of the black hole χ_{eff} , the baryonic mass of the neutron star M_{NS}^* , the quotient of the neutron star’s gravitational mass M_{NS} and baryonic mass M_{NS}^* , and its compactness C , i.e., five parameters. For the case of BNS systems, the number increases to six: the gravitational masses M_1, M_2 , the baryonic masses M_1^*, M_2^* , and the compactnesses C_1, C_2 of the neutron stars.

As an example to visualize possible degeneracies in Equations (1)–(7), let us suppose that the ejecta mass and the ejecta velocity were measured for a BHNS setup. In Figure 10, we show as red surfaces the allowed binary parameters for which $M_{\text{ej}} = 10^{-2}$ under the assumptions of $C = 0.13, 0.15, 0.17$. In addition, we make use of the quasi-universal relation given by Equation (8) (see discussion in the next subsection) to connect the gravitational and baryonic mass to the compactness. As a blue surface, we mark the binary parameters for which $v_{\text{ej}} = 0.28$. According to Equation (2), the measurement of v_{ej} would determine the mass ratio of the system q but leave the other parameters unconstrained.

Figure 10 shows that even if M_{ej} and v_{ej} are accurately known, the binary parameters cannot be determined. The intersections between the red and blue surfaces mark all the allowed regions for which the ejecta properties are consistent with the estimated $M_{\text{ej}}, v_{\text{ej}}$ under the assumption of a given compactness C . Consequently, an accurate measurement of the binary properties is only possible for cases for which more parameters than $M_{\text{ej}}, v_{\text{ej}}$ are determined, e.g., θ_{ej} and ϕ_{ej} , or for cases where, due to a simultaneous detection of GWs, some binary parameters are known.

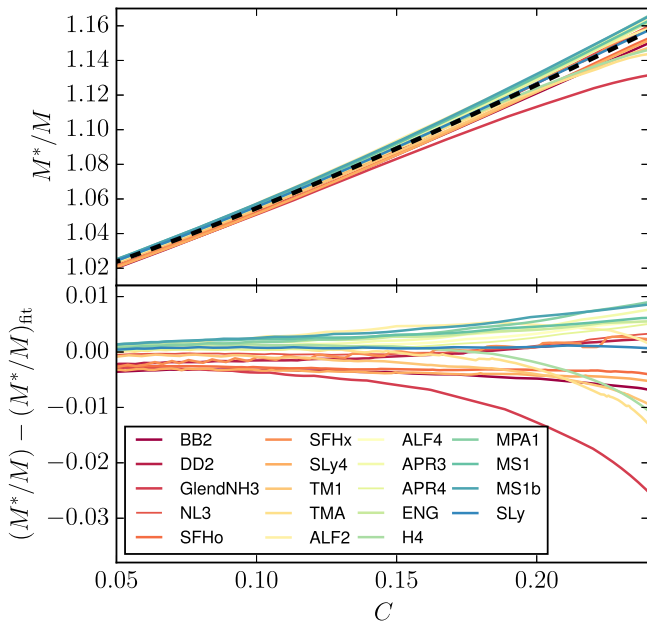


Figure 11. Ratio of the baryonic mass and gravitational mass M^*/M as a function of the compactness for different equations of state (top panel) and the difference for M^*/M between each EOS and the approximant Equation (8) (bottom panel). The dashed black line corresponds to the fit.

5.2. Quasi-universal Properties

Due to the large number of unknown binary parameters in Equations (1)–(7), several degeneracies exist and binary parameters cannot be constrained uniquely. To reduce this effect, we substitute some parameters with the help of quasi-universal relations. Quasi-universal properties for single neutron stars have been first found by Yagi & Yunes (2013) and were consequently studied for a variety of parameters (see, e.g., Maselli et al. 2013; Pappas & Apostolatos 2014; Yagi et al. 2014); even in BNS systems quasi-universal relations are present (e.g., Bernuzzi et al. 2014). We propose a relation between the quotient of baryonic and gravitational mass M^*/M and the compactness C of a single neutron star. To construct this relation, we use the EOSs employed for the data set studied in Dietrich & Ujevic (2017) but only consider EOSs that allow nonrotating NS masses above 1.9, which lies even below the highest measured NS mass of ≈ 2.01 . Figure 11 shows M^*/M as a function of the compactness C for all EOSs. We find that only a small spread is caused by the EOSs. Except for GlendNH3, all curves stay close together.

We fit all data with an approximant of the form

$$\frac{M^*}{M} = 1 + a C^n, \quad (8)$$

where the free fitting parameters are $a = 0.8858$ and $n = 1.2082$. The fit is included as a black dashed line in the top panel of Figure 11. By construction, we obtain for $C \rightarrow 0$ the correct limit of $M^*/M \rightarrow 1$. The residuals of the fit are shown in the bottom panel of Figure 11. Absolute errors within the compactness interval of $C \in [0.05, 0.24]$ are within ± 0.01 , except for GlendNH3. This leads to fractional errors of $\lesssim 10\%$ for the term $1 - M^*/M$, which enters directly in the ejecta mass computation for BHNS and BNS systems. On average, fractional errors are $\lesssim 3\%$. Considering the large uncertainty of Equations (1)–(7), we expect that the error caused by

Equation (8) is negligible. But by introducing this relation, the number of free parameters for the BHNS model is reduced by one and for the BNS model is reduced by two. This allows for significantly better extraction of the binary parameters from the ejecta properties.

5.3. Extraction of Binary Parameters

In the following, we use a similar scheme to that in Section 4 to explore how binary parameters can be recovered from a kilonova detection. We explore the situation where we have made a measurement of M_{ej} and v_{ej} . We calculate the likelihood using a kernel density estimator commonly used in GW data analysis (Singer et al. 2014). This technique is useful for cases where the measurements of those distributions arise from parameter estimation with potentially highly correlated estimates among the variables, as is common in GW data analysis. The priors used in the analyses are as follows: for Kawaguchi et al. (2016), $3 \leq q \leq 9$, $0 \leq \chi_{\text{eff}} \leq 0.75$, $1 \leq M_{\text{NS}} \leq 3$, and $0.1 \leq C \leq 0.2$, while for Dietrich & Ujevic (2017), $1 \leq M_1 \leq 3$, $1 \leq M_2 \leq 3$, $0.08 \leq C_1 \leq 0.24$, and $0.08 \leq C_2 \leq 0.24$. The differences in compactness prior ranges are due to the differences in compactness used in the simulations the models used. The priors are flat over the stated ranges. For this reason, significant structure in the 1D and 2D contours arises from the posterior.

To begin, we explore the correlation between the variables by employing the very optimistic assumption of 1% Gaussian error bars on the measurement, which essentially inverts the equations in the previous section. We show in Figure 12 the parameters consistent with two different choices of M_{ej} and v_{ej} . For the BNS case (left panel), we choose $M_{\text{ej}} = 5 \times 10^{-3}$ and $v_{\text{ej}} = 0.25$; for the BHNS case (right panel), we choose $M_{\text{ej}} = 5 \times 10^{-2}$ and $v_{\text{ej}} = 0.25$. In general, for the BNS systems, the constraints are not strong given the relatively wide variety of parameters that support nonzero ejecta masses and velocities. We choose to plot mass ratio ($q = M_1/M_2$) and chirp mass ($M_c = (M_1 M_2)^{3/5} (M_1 + M_2)^{-1/5}$) instead of M_1 and M_2 , due to the clearer peaks in this parameterization. We clearly see in the 2D corner plots degeneracies between M_c and q , as well as between C_1 and C_2 , which are similar to those described in the previous subsection. These indicate the fundamental limitations of EM-only observations in the measurements of these quantities. For the BHNS systems, the main constraint is on q , which has some correlation with compactness. Due to the significant correlations between q , χ_{eff} , and C , it will be difficult to constrain those individual parameters without measurements from other quantities. The degeneracies can be broken by using assumptions based on priors based on the measured masses of BNS systems, the spins of binary black holes, or the compactness of neutron stars, or indeed, these quantities as measured by coincident GW observations.

Figure 13 shows more realistic levels of parameter estimates using the M_{ej} and v_{ej} contours sampled from a light curve with $M_{\text{ej}} \approx 5 \times 10^{-3}$ and $v_{\text{ej}} \approx 0.2$ with model uncertainties of 0.2 mag. The main difference between these results and the optimistic assumptions above are the relatively poor constraints on v_{ej} . For the BNS system (left panel), because the constraints on mass ratio are tied to v_{ej} , most values of mass ratio are allowed in this particular case. There are only minimal constraints on M_c , C_1 , and C_2 . For the BHNS system (right

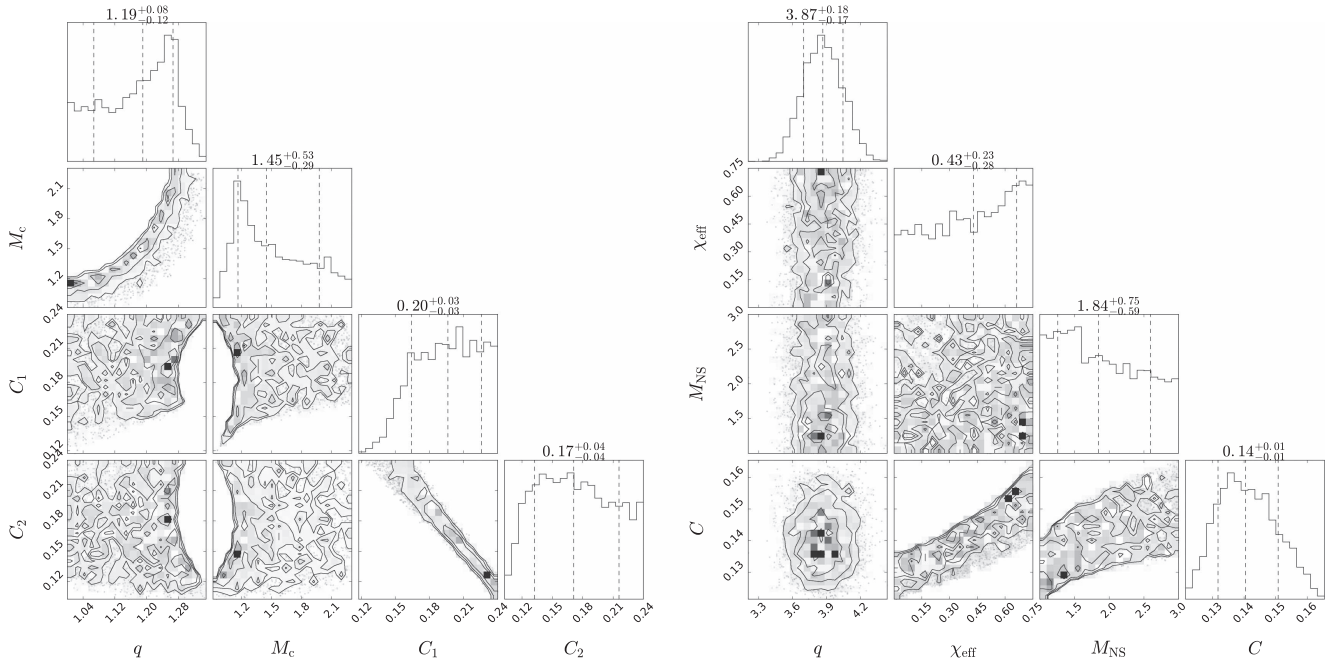


Figure 12. Left: corner plot for the model fits for the Dietrich & Ujevic (2017) model with $M_{\text{ej}} = 5 \times 10^{-3}$, $v_{\text{ej}} = 0.25$, and an optimistic 1% Gaussian error bar on the measurement. Right: same as the left panel, but for the Kawaguchi et al. (2016) model with $M_{\text{ej}} = 5 \times 10^{-2}$ and $v_{\text{ej}} = 0.25$ for comparison with the same error bars.

panel), the only structure visible is the correlation between q , χ_{eff} , and C . In the case of precise measurement of the mass ratio and effective spin by GW parameter estimation, constraints on the neutron star compactness of $C \pm 0.2$ are possible.

As a final comparison, we perform parameter estimation for the Dietrich & Ujevic (2017) model with 0.2 mag uncertainty, but instead of sampling in M_{ej} and v_{ej} , we sample directly in the system parameters making use of Equations (3)–(7). Figure 14 shows the corner plots for this scenario. We find that the individual binary parameters are almost undetermined; only in the 2D M_1 – M_2 or, as shown in the figure, the M_c – q plane is a clear contour visible. According to the 1D posteriors of q , it seems that high mass ratios are ruled out. Additionally, C_1 , C_2 are almost unconstrained, but there seems to be a small preference for larger compactnesses for the shown example.

Although we have only discussed the extraction of binary parameters for BNS configurations, similar results are obtained for BHNS systems.

6. Synergy of Electromagnetic and GW Observations

As described in the previous section, the constraints on M_c and q from EM observations alone are limited. On the other hand, GW parameter estimation provides direct constraints on these quantities as well. In particular, M_c is strongly constrained (Abbott et al. 2016b, 2016c, 2017). Previously, the idea of using EM transients as triggers in searches for GWs from compact binary mergers was proposed (Kelley et al. 2013). Also, the possibility of combining host galaxy identification with GW parameter estimation to yield improved constraints on binary inclination has been mentioned before (Fan et al. 2014). Additionally, we can use information from the GW parameter estimation combined with constraints from the EM parameter estimation to improve limits on the ejecta properties.

To demonstrate the benefits of this kind, we take an example from Singer et al. (2014), which includes both GW skymaps and posteriors from the parameter estimation of BNS signals. We take one such example and generate a light curve using the Dietrich & Ujevic (2017) model corresponding to the mean of the mass posteriors with compactnesses of $C_{1,2} = 0.147$ and use the quasi-universal relation, Equation (8), to compute the baryonic masses. The true values are $M_{\text{ej}} = 0.006$ and $v_{\text{ej}} = 0.2$. We use magnitude uncertainties of 1.0 and 0.2 mag.

We perform the same parameter estimation technique as in the previous sections to derive EM-only constraints on M_{ej} and v_{ej} . We then use the GW parameter estimation posteriors of M_1 and M_2 to derive GW-only constraints on M_{ej} and v_{ej} . This is accomplished by using a kernel density estimator on the GW posteriors of M_1 and M_2 and allowing C_1 and C_2 to vary using the same priors as with the EM parameter estimation. Combining these posteriors is performed straightforwardly by multiplying the probabilities derived from both the GW-only and the EM-only posteriors, but note that because we are multiplying 2D probabilities from correlated variables, the marginalized posteriors from the combined analysis can look different from multiplying the 1D marginalized distributions.

In Figure 15, we show histograms for M_{ej} , v_{ej} , M_c , and q for EM-only (green), GW-only (blue), and combined EM–GW (red) constraints. The figure demonstrates that significant improvements are possible with joint EM and GW parameter estimation. For example, whereas there are almost no limits on v_{ej} with EM only, constraints from GW parameter estimation create a clear peak in the posterior and the ejecta velocity can be determined up to $v_{\text{ej}} \approx \pm 0.15$. The limits on M_{ej} show the true synergy between potential EM and GW parameter estimation. The broad posteriors of the EM-only and GW-only constraints are narrowed when combined, e.g., for an uncertainty of 1.0 mag the uncertainty decreases from $\log_{10} M_{\text{ej}} \approx \pm 0.75$ to $\log_{10} M_{\text{ej}} \approx \pm 0.4$. In the case where a magnitude uncertainty of 0.2 mag is employed, the constraints on velocity are still dominated by the GW parameter

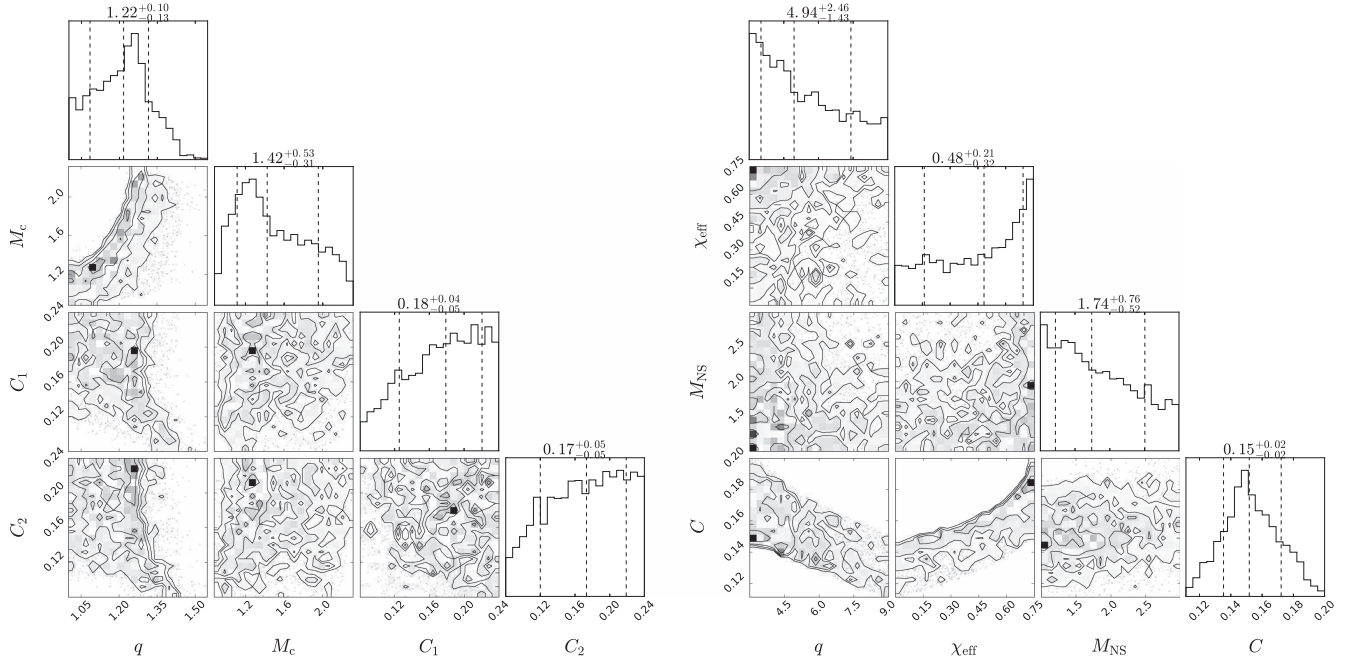


Figure 13. Left: corner plot for the model fits for the Dietrich & Ujevic (2017) model for M_{ej} and v_{ej} contours sampled from a light curve with $M_{\text{ej}} \approx 5 \times 10^{-3}$, $v_{\text{ej}} \approx 0.2$ (similar to Figure 12), and model uncertainties of 0.2 mag. Right: same as the left panel, but for the Kawaguchi et al. (2016) model for comparison.

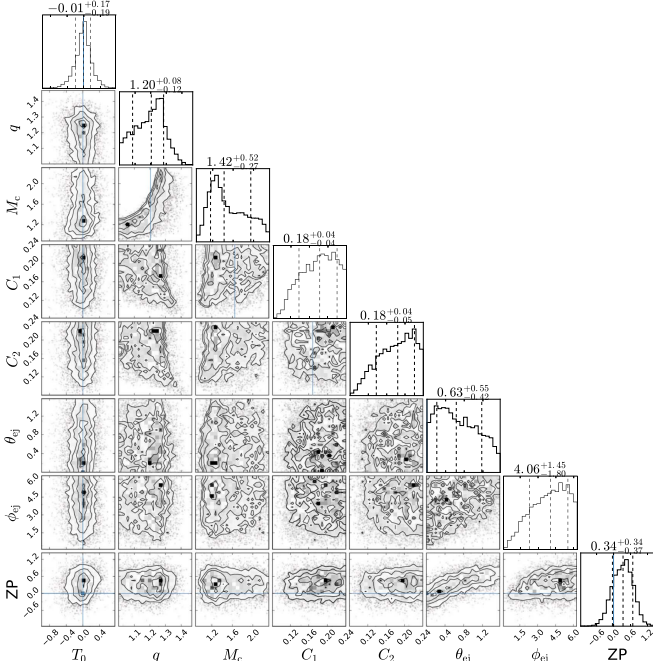


Figure 14. Corner plots for light curves with $M_{\text{ej}} = 5 \times 10^{-3}$, $v_{\text{ej}} = 0.2$, $\theta_{\text{ej}} = 0.2$ rad, and $\phi_{\text{ej}} = 3.14$ rad using the Dietrich & Ujevic (2017) model with 0.2 mag uncertainty.

estimation, but the M_{ej} determination is dominated by the EM measurement.

Considering the binary parameters, we find that for 0.2 and 1.0 mag the chirp mass M_c is purely constrained by the GW parameter estimation. On the other hand, while for a magnitude uncertainty of 1 mag the mass ratio is mostly determined by GW parameter estimation with only minor improvement once EM parameter estimation is also considered, one finds that for magnitude uncertainty of 0.2 mag constraints are improved and decrease from $q \approx \pm 0.25$ to $q \approx \pm 0.2$. Due to the minimal

correlation between M_c , q , and the compactnesses, improved constraints on the compactnesses are not expected. It is important to note that there is no bias in the measurement of q in the GW–EM case. The 1D posterior for q shifts left as the EM error bars are reduced owing to the significant correlation between M_c and q from the parameter estimation, as can be seen from the left panel of Figure 13.

We now perform an analysis similar to that above using a BHNS example from Littenberg et al. (2015), using the Kawaguchi et al. (2016) model to generate light curves with $M_{\text{ej}} = 0.1$ and $v_{\text{ej}} = 0.25$ with magnitude uncertainties of 1.0 and 0.2 mag. We once again use the mass posteriors from the GW parameter estimation and allow the effective spin χ_{eff} and the neutron star compactness C to vary. In Figure 16, we show histograms for M_{ej} , v_{ej} , M_c , and q for EM-only (green), GW-only (blue), and combined EM–GW (red) constraints. Similar to the BNS case, there are improvements to be made with joint EM and GW parameter estimation. While v_{ej} is once again constrained by GW observations, the posteriors of M_{ej} are narrowed when GW and EM are combined, e.g., for an uncertainty of 1.0 mag the uncertainty decreases from $\log_{10} M_{\text{ej}} \approx \pm 1.0$ to $\log_{10} M_{\text{ej}} \approx \pm 0.5$. The improvement is similar in the case where a magnitude uncertainty of 0.2 mag is employed. Similar to the BNS case, the chirp mass M_c constraints are dominated by the GW observation, while improvements for mass ratio q are seen. Unlike in the BNS case, the GW and EM constrain different regimes for q , with EM covering $3 \leq q \leq 8$ and GW covering $5 \leq q \leq 9$, resulting in a combined GW–EM constraint of $5 \leq q \leq 8$.

In summary, the presence of a kilonova coincident with a GW observation can be used to constrain the source properties better than either GW or EM individually. First of all, the presence of a detectable kilonova provides evidence of unbound material and therefore can constrain GW inference by removing those samples that support little or no ejecta. Second, by comparing the measured light curves to that predicted by the light-curve models, these parameters can be

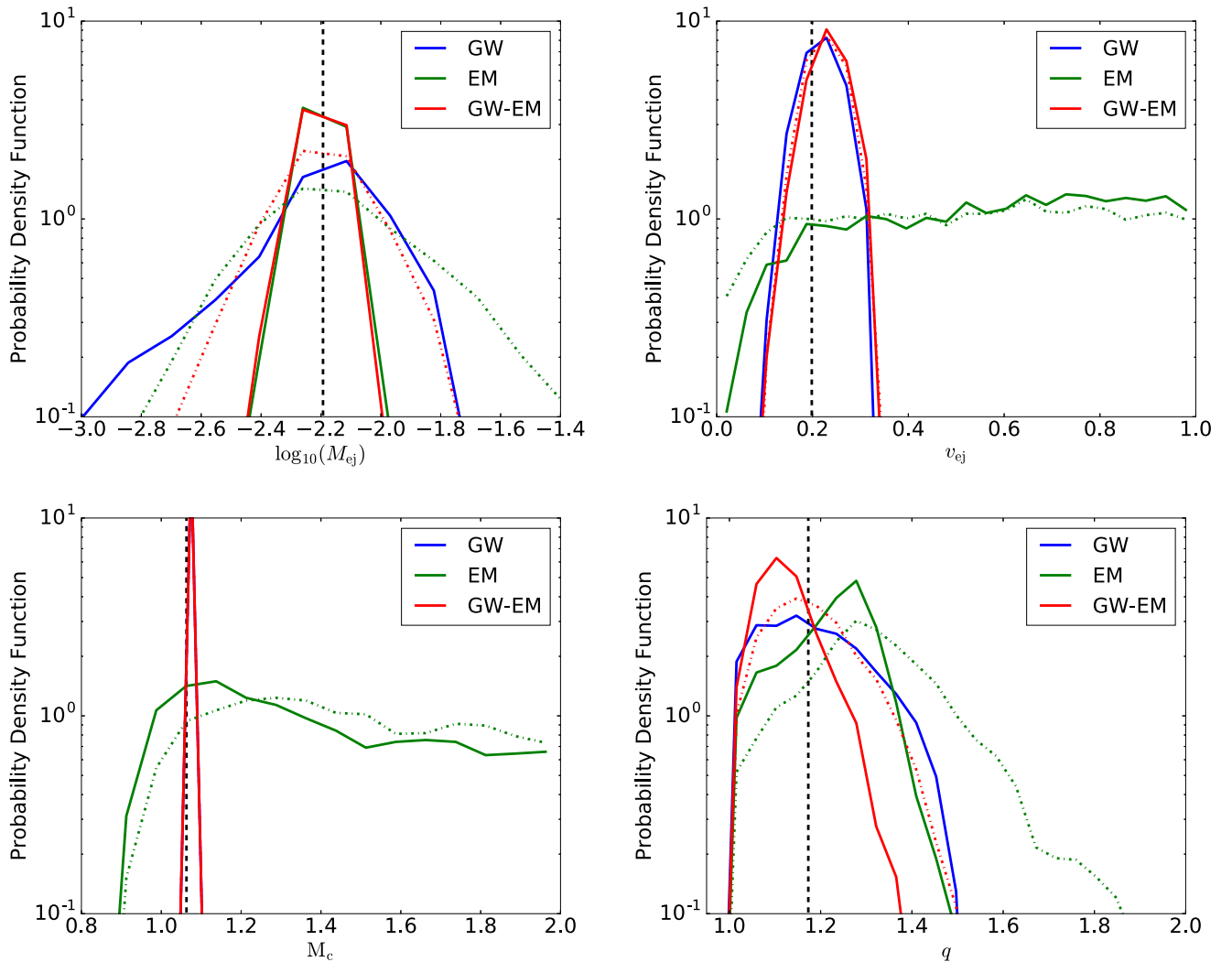


Figure 15. Histograms of M_{ej} (top left), v_{ej} (top right), M_c (bottom left), and q (bottom right) for EM-only, GW-only, and combined EM–GW constraints on a simulated BNS with GW parameter estimation from Singer et al. (2014). Parameter estimation using a simulated light curve from the Dietrich & Ujevic (2017) model consistent with this simulated BNS was used to generate the EM constraints. For this analysis we assume 0.2 mag (solid lines) and 1 mag (dot-dashed lines) uncertainties of the kilonova model. The injected (true) value is marked as a vertical dashed line. In the case of M_c , the GW-only line lies directly below the GW–EM line.

constrained. In general, M_c and v_{ej} can be constrained by GW parameter estimation, with little improvement from the inclusion of EM results. On the other hand, with the uncertainty budgets of current kilonova models and relations between binary parameters and ejecta properties, combined GW–EM parameter estimation improves possible constraints for both M_{ej} and q . While it is true that in a future where kilonova models have improved such that their uncertainties are at the order of observation level, the EM observations will dominate the M_{ej} and q constraints, and therefore a combined analysis would not be useful; however, it is unlikely that such big improvements can be made in the near future. This motivates the importance for coordination between GW and EM parameter estimation in the event of a kilonova counterpart detection.

7. Conclusion

In this article, we compared different light-curve models, outlined differences and similarities, and checked the consistency among the models. We showed how parameter

estimation based on the kilonova light curves depends on the uncertainty of the employed models.

We found that the parameterized models of Kawaguchi et al. (2016) and Dietrich & Ujevic (2017) are able to recover the light curves and parameters of the radiative transfer simulations of Tanaka et al. (2014). As we have shown in Figures 5 and 6, the ejecta properties can be determined accurately once the models have small uncertainty, e.g., an estimate of the ejecta mass of $\log_{10} M_{ej} \approx \pm 0.5$ could be obtained once the model’s uncertainty is below 0.2 mag. We find that currently both the Kawaguchi et al. (2016) and Dietrich & Ujevic (2017) models are consistent with their stated uncertainties (and Kawaguchi et al. [2016] perhaps even better than that) and that there are significant gains in parameter estimation to be made when these uncertainties decrease. We hypothesize that for updated simulations using more detailed microphysical descriptions, in particular a better treatment of weak interaction, i.e., neutrino physics, it would also be possible to produce analytic models for the results of NR and radiative transfer simulations. With a model that both describes the improved simulations and has

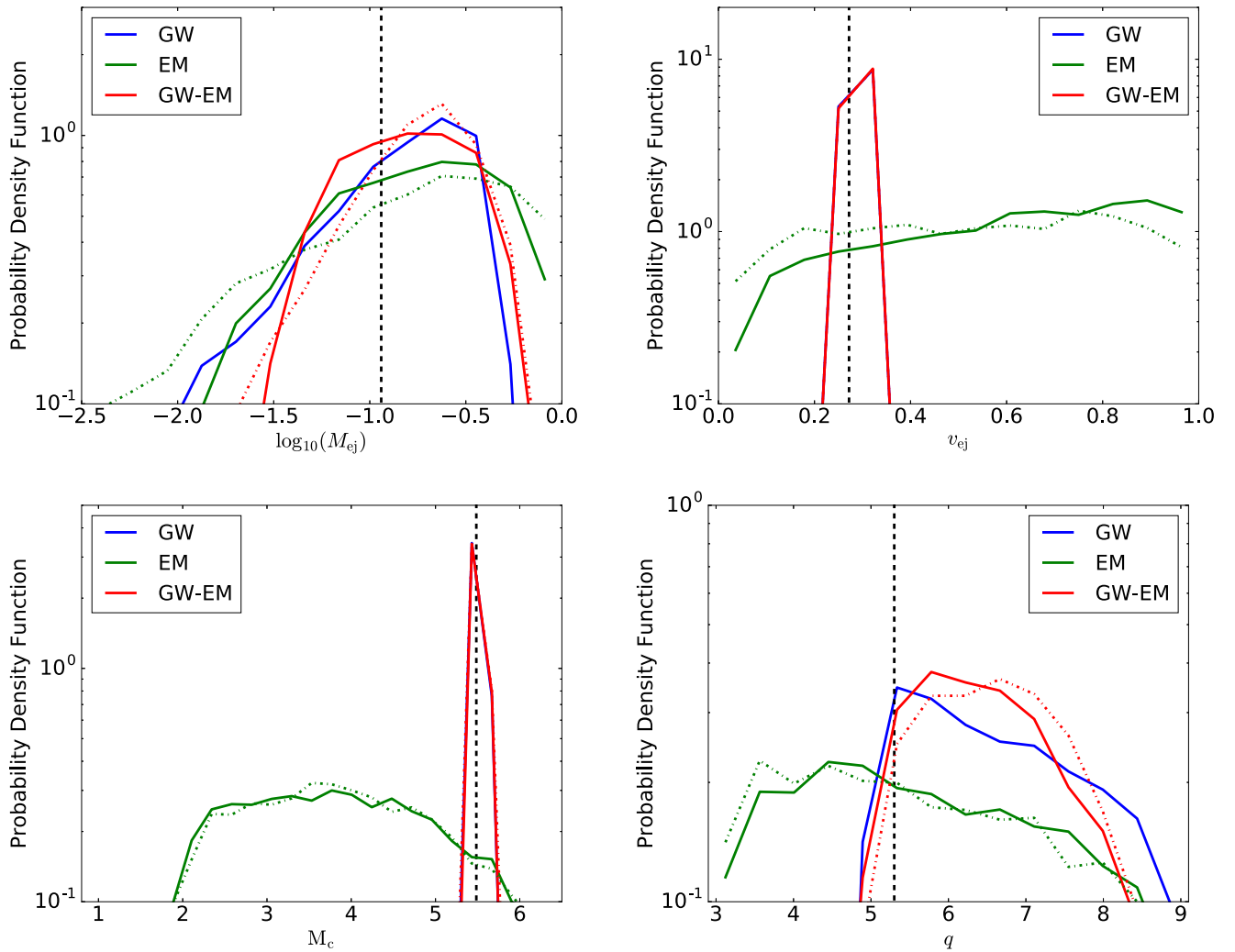


Figure 16. Histograms of M_{ej} (top left), v_{ej} (top right), M_c (bottom left), and q (bottom right) for EM-only, GW-only, and combined EM–GW constraints on a simulated BHNS with GW parameter estimation from Littenberg et al. (2015). Parameter estimation using a simulated light curve from the Kawaguchi et al. (2016) model consistent with this simulated BHNS was used to generate the EM constraints. For this analysis we assume 0.2 mag (solid lines) and 1 mag (dot-dashed lines) uncertainties of the kilonova model. The injected (true) value is marked as a vertical dashed line. In the case of M_c , the GW-only line lies directly below the GW–EM line.

smaller inherent uncertainties in hand, it is in principle possible to make precision measurements of ejecta mass with results limited only by observation.

To improve the parameter estimation and allow for an extraction of the binary properties, we introduced a quasi-universal relation between the quotient of baryonic and gravitational mass M^*/M and the compactness C of a single neutron star. This relation reduced the number of free parameters for the parameter estimation and consequently improved the extraction of the individual binary parameters. We also compared the parameterized models with other kilonova models and light curves of other transients. As expected, the light curves of a blue kilonova precursor and an SN Ia cannot be approximated by the models, which shows that the parameterized models could also be used to rule out some of the possible measured transients. We also found that other kilonova light curves, Barnes et al. (2016) and Rosswog et al. (2017), are not accurately described as well. This is caused by the difference in the underlying radiative transfer simulations on which the models are built, which emphasizes again the need to improve and update kilonova models in the future.

We also showed how to include the posterior samples from GW signals from a BNS or BHNS to give further constraints on parameters for the light curves. We showed improved constraints on the ejecta properties M_{ej} , v_{ej} and the binary parameters M_c , q using a combination of GW and EM observations. This motivates combined analysis in the case of a kilonova detection coincident with a GW trigger.




However, a number of hurdles remain. Mostly due to the large uncertainties in the ejecta mass, velocity, and density profile, the effect of thermal efficiency, and the estimated opacity in the ejected material, there are large biases, and parameter estimation with the current existing models is hampered. To overcome these issues, improvements have to be made in NR by performing longer simulations that include additional physics such as other ejecta components from magnetic-driven winds or neutrino outflows (see, e.g., Surman et al. 2008; Metzger et al. 2008; Dessart et al. 2009; Perego et al. 2014). Additionally, improved radiative simulations will be needed. Based on those simulations, new parameterized models could be developed in the future.

For future application, it will also be useful to consider how to implement a search strategy in existing data sets when the light curves are not necessarily well sampled. This would optimize the tiling and time allocation strategies of existing searches for GW counterparts with telescopes with wide fields of view.

A code to produce the results in this paper is available at <https://github.com/mcoughlin/gwemlightcurves> for public download. Required for analysis are text files of light curves from models of interest in magnitudes, typically available from groups developing kilonova models. Furthermore, the kilonova model of Kawaguchi et al. (2016) can be found online at www2.yukawa.kyoto-u.ac.jp/~kyohei.kawaguchi/kn_calc/main.html, and the model of Dietrich & Ujevic (2017) can be found at <http://www.aei.mpg.de/~tdietrich/kn/main.html>.

The authors would like to thank Zoheyr Doctor for a careful reading of an earlier version of the manuscript. M.C. is supported by National Science Foundation Graduate Research Fellowship Program, under NSF grant no. DGE 1144152. C.S. is grateful to the DOE Office of Science for their support under award DE-SC0007881. M.U. is supported by Fundação de Amparo à Pesquisa do Estado de São Paulo (FAPESP) under the process 2017/02139-7. K.K. is supported by JSPS Postdoctoral Fellowships for Research Abroad.

ORCID iDs

Michael Coughlin  <https://orcid.org/0000-0002-8262-2924>
 Stephen Smartt  <https://orcid.org/0000-0002-8229-1731>
 Christopher Stubbs  <https://orcid.org/0000-0003-0347-1724>

References

- Abbott, B. P., Abbott, R., Abbott, T. D., et al. 2016a *ApJL*, **826**, L13
 Abbott, B. P., Abbott, R., Abbott, T. D., et al. 2016b *PhRvL*, **116**, 061102
 Abbott, B. P., Abbott, R., Abbott, T. D., et al. 2016c *PhRvL*, **116**, 241103
 Abbott, B. P., Abbott, R., Abbott, T. D., et al. 2017, *PhRvL*, **118**, 221101
 Barnes, J., & Kasen, D. 2013, *ApJ*, **775**, 18
 Barnes, J., Kasen, D., Wu, M.-R., & Martínez-Pinedo, G. 2016, *ApJ*, **829**, 110
 Bernuzzi, S., Nagar, A., Balmelli, S., Dietrich, T., & Ujevic, M. 2014, *PhRvL*, **112**, 201101
 Berry, C. P. L., Mandel, I., Middleton, H., et al. 2015, *ApJ*, **804**, 114
 Buchner, J., Georgakakis, A., Nandra, K., et al. 2014, *A&A*, **564**, A125
 Cowperthwaite, P. S., & Berger, E. 2015, *ApJ*, **814**, 25
 Dessart, L., Ott, C., Burrows, A., Rosswog, S., & Livne, E. 2009, *ApJ*, **690**, 1681
 Dietrich, T., & Ujevic, M. 2017, *CQGra*, **34**, 105014
 Doctor, Z., Kessler, R., Chen, H. Y., et al. 2017, *ApJ*, **837**, 57
 Duflo, J., & Zuker, A. P. 1995, *PhRvC*, **52**, R23
 Fairhurst, S. 2009, *NJPh*, **11**, 123006
 Fairhurst, S. 2011, *CQGra*, **28**, 105021
 Fan, X., Messenger, C., & Heng, I. S. 2014, *ApJ*, **795**, 43
 Feroz, F., Gair, J. R., Hobson, M. P., & Porter, E. K. 2009a, *CQGra*, **26**, 215003
 Feroz, F., Hobson, M. P., & Bridges, M. 2009b, *MNRAS*, **398**, 1601
 Foreman-Mackey, D. 2016, *JOOS*, **24**
 Grover, K., Fairhurst, S., Farr, B. F., et al. 2014, *PhRvD*, **89**, 042004
 Guy, J., Astier, P., Baumont, S., et al. 2007, *A&A*, **466**, 11
 Ivezić, Z., Tyson, J. A., Allsman, R., Andrew, J., & Angel, R. 2008, arXiv:0805.2366
 Kasen, D., Badnell, N. R., & Barnes, J. 2013, *ApJ*, **774**, 25
 Kasen, D., Fernandez, R., & Metzger, B. 2015, *MNRAS*, **450**, 1777
 Kasliwal, M. M., Cenko, S. B., Singer, L. P., et al. 2016, *ApJL*, **824**, L24
 Kawaguchi, K., Kyutoku, K., Shibata, M., & Tanaka, M. 2016, *ApJ*, **825**, 52
 Kelley, L. Z., Mandel, I., & Ramirez-Ruiz, E. 2013, *PhRvD*, **87**, 123004
 Kisaka, S., Ioka, K., & Takami, H. 2015, *ApJ*, **802**, 119
 Kulkarni, S. R. 2005, arXiv:astro-ph/0510256
 Kyutoku, K., Ioka, K., & Shibata, M. 2014, *MNRAS*, **437**, L6
 Levermore, C. D., & Pomraning, G. C. 1981, *ApJ*, **248**, 321
 Li, L.-X., & Paczynski, B. 1998, *ApJL*, **507**, L59
 Littenberg, T. B., Farr, B., Coughlin, S., Kalogera, V., & Holz, D. E. 2015, *ApJL*, **807**, L24
 Maselli, A., Cardoso, V., Ferrari, V., Gualtieri, L., & Pani, P. 2013, *PhRvD*, **88**, 023007
 Metzger, B. D. 2017, *LRR*, **20**, 3
 Metzger, B. D., Bauswein, A., Goriely, S., & Kasen, D. 2015, *MNRAS*, **446**, 1115
 Metzger, B. D., & Berger, E. 2012, *ApJ*, **746**, 48
 Metzger, B. D., Martínez-Pinedo, G., Darbha, S., et al. 2010, *MNRAS*, **406**, 2650
 Metzger, B. D., Quataert, E., & Thompson, T. A. 2008, *MNRAS*, **385**, 1455
 Moller, P., Nix, J. R., Myers, W. D., & Swiatecki, W. J. 1995, *ADNDT*, **59**, 185
 Morgan, J. S., Kaiser, N., Moreau, V., Anderson, D., & Burgett, W. 2012, *Proc. SPIE*, **8444**, 84440H
 Nakar, E. 2007, *PhR*, **442**, 166
 Pappas, G., & Apostolatos, T. A. 2014, *PhRvL*, **112**, 121101
 Perego, A., Rosswog, S., Cabezón, R. M., et al. 2014, *MNRAS*, **443**, 3134
 Rau, A., Kulkarni, S. R., Law, N. M., et al. 2009, *PASP*, **121**, 1334
 Rosswog, S. 2015, *IJMPD*, **24**, 1530012
 Rosswog, S., Feindt, U., Korobkin, O., et al. 2017, *CQGra*, **34**, 104001
 Sidery, T., Aylott, B., Christensen, N., et al. 2014, *PhRvD*, **89**, 084060
 Siegel, D. M., & Metzger, B. D. 2017, arXiv:1705.05473
 Singer, L. P., Price, L. R., Farr, B., et al. 2014, *ApJ*, **795**, 105
 Smartt, S. J., Chambers, K., Smith, K., et al. 2016a, *MNRAS*, **462**, 4094
 Smartt, S. J., Chambers, K. C., Smith, K. W., et al. 2016b, *ApJL*, **827**, L40
 Stalder, B., Tonry, J., Smartt, S. J., et al. 2017, arXiv:1706.00175
 Surman, R., McLaughlin, G. C., Ruffert, M., Janka, H.-T., & Hix, W. R. 2008, *ApJL*, **679**, L117
 Tanaka, M. 2016, *AdAst*, **2016**, 6341974
 Tanaka, M., & Hotokezaka, K. 2013, *ApJ*, **775**, 113
 Tanaka, M., Hotokezaka, K., Kyutoku, K., et al. 2014, *ApJ*, **780**, 31
 Tonry, J. L. 2011, *PASP*, **123**, 58
 Wen, L., & Chen, Y. 2010, *PhRvD*, **81**, 082001
 Yagi, K., Stein, L. C., Pappas, G., Yunes, N., & Apostolatos, T. A. 2014, *PhRvD*, **90**, 063010
 Yagi, K., & Yunes, N. 2013, *Sci*, **341**, 365